Article:

Chi, Y, Xu, L and Yu, H-S (2014) Plasticity Model for Hybrid Fiber-Reinforced Concrete under True Triaxial Compression. Journal of Engineering Mechanics, 140 (2). pp. 393-405. ISSN 0733-9399

https://doi.org/10.1061/(ASCE)EM.1943-7889.0000659

Plasticity Model for Hybrid Fiber Reinforced Concrete under True Triaxial Compression

[1]Yin Chi, [2]Lihua Xu, [3]Hai-Sui Yu

Abstract: Based on the experimental background of 75 true triaxial compression tests conducted on cubic specimens, a plasticity constitutive model for hybrid steel-polypropylene fiber reinforced concrete (HFRC) is developed in this study, aiming to accurately predict the strength and deformation of HFRC under various loading scenarios. A five-parameter Willam-Warnke failure surface is modified to account for the presence of hybrid fibers. The evolution of the loading surface is characterized by uncoupled hardening and softening regimes determined by the accumulated equivalent plastic strain, and a Drucker-Prager non-associated plastic flow is used to describe the plastic deformation. Various model parameters are mainly calibrated on the basis of true triaxial compression test data. Subsequently, the responses of the constitutive model are verified by multiaxial compression test results of both plain concrete and fiber reinforced concrete reported by various researchers. It is observed that a good estimation of the strength and the deformation capacity of HFRC with varying fiber volume fractions and aspect ratios can be achieved by the proposed model.

CE Database subject headings: Plasticity; Constitutive modeling; Fiber reinforced; Concrete; Strength; Compression;

Introduction

Relatively recent advances in concrete technology have led to the development of fiber reinforced concrete (FRC), which is now recognized by engineers as a viable concrete reinforcement solution and has seen widespread application in the construction industry in recent decades. With the increasing use

1, Ph.D, NCG, The University of Nottingham, evxyc4@nottingham.ac.uk, C10 Coates Building, The University of Nottingham, University Park, Nottingham,NG72RD.
2, Professor, School of Civil Engineering, Wuhan University, xulihua-d@126.com, 8 South Road of East Lake, Wuhan University, WuChang district, 430072.
3, Professor, NCG, The University of Nottingham, hai-sui.yu@nottingham.ac.uk, Coates Building, The University of Nottingham, University Park, Nottingham,NG72RD.

of FRC as a primary structural material in building complex structures such as reactor vessels, dams and offshore structures(ACI Committee 544, 1982; Swamy and Barr, 1989;Bentur and Mindess, 1990)., it has become necessary to develop a sophisticated analytical model capable of accurately describing FRC behavior when it is subjected to various loading scenarios.

To date, considerable efforts have been geared towards advancing the development of constitutive models for plain concrete as well as high strength concrete(e.g., Chen and Han,1985; Belarbi and Hsu,1995; Ansari and Li, 1998; Attard and Setunge,1996; Hussein and Marzouk, 2000;Babu et al., 2006;Grassl et al., 2002). Constitutive models with various theories, i.e, plasticity models, damage models, microplane models, discrete models, or models with coupling theories etc., have been extensively researched and well acknowledged, which are capable of effectively capturing the behavioral characteristics of concrete materials. Using existing traditional concrete models as a foundation, different methods and formulations for constitutive modeling of FRC materials have been proposed with SFRC in particular, and have been extensively researched in literature. However, it has been noted that some of the models are only suited to specific loading paths (e.g. Nataraja et al., 1999; Hsu and Hsu, 1994; Murugappan et al., 1993; Hu et al., 2003). Other models considered to have been obtained through phenomenological or empirical methods have no systematic expression formulated to predict the model’s response to variations in the fiber reinforcement index(FRI, which is calculated by multiplying fiber volume fraction and its aspect ratio) (e.g. Chern et al., 1992; Lu et al., 2006). Consequently, comparisons between test data and numerical simulations of complex problems often revealed poor predictive capability of the numerical models owing to inadequate theoretical description of the FRC materials. In such an instance, the proposed constitutive model may not degenerate back to the case of conventional concrete as the fiber vanishes. The simulation results by using such model may lead to a lack of confidence in computational analysis of structural responses for the cases where significant material nonlinearities are involved.

A review of existing literature indicated that although previous FRC investigations appears to have been concentrated on the constitutive modeling of SFRC and HFRC, only the influence of different volume fraction (e.g.,Yin et al., 1989; Traina and Mansor, 1991;Yun et al., 2007; Di Prisco et al., 2009) was considered. Of the limited research available on the development of a constitutive model for HFRC with various fiber reinforcement indices, it is found that the performance of FRC is sensitive to changes in both the fiber volume fractions and aspect ratios.

In view of the above mentioned, it is clear that significant advancement of knowledge is required to facilitate the behavioral characterization of HFRC subjected to multiaxial compressive loading situations. The subsequent focus of this study is therefore to develop a plasticity constitutive model to take into account the presence of various hybrid fibers of HFRC. True triaxial tests are carried out to calibrate various model parameters, and the developed model is implemented into general FE package ABAQUS by UMAT subroutine via an explicit integration algorithm, the model's performance is then evaluated by available experimental data.

Experimental Program

Materials and mix proportions

The plain concrete mixtures were designed and specified at a 28-day compressive strength of 60MPa. Ordinary Portland cement (P.O 42.5) was used as the binder for the mixtures. Crushed granitic rocks of sizes between 5~20mm were used as the coarse aggregates. Normal river sand including 5% of water (by weight) with fineness modulus of 2.7 was used as the fine aggregates. A highly efficient water reducing agent with a reducing rate of about 20% was used in the mix design. The mix design by weight of the plain concrete mixture was in the ratio 1:0.34:1.80:2.49 (cement:water:sand:coarse aggregate) and designed according to literature (GB/T50081-2002).

For steel fiber, to make the full use of the advantage in strength improvement and toughness, the volume fraction of steel fiber is suggested between 0.5% and 2.0% and the aspect ratio is suggested between 30 and 80 according to literature (CECS 2004). Therefore, corrugated steel fibers produced by WuHan Hansen Steel Fiber Ltd (Fig.1) with the tensile strength over 600MPa were used in volume fractions of 0.5%, 1% and 1.5% in this study, and the fiber aspect ratios (length/diameter) of 30, 60 with a fixed diameter of 0.5mm were employed.

For polypropylene fiber, according to the product instruction, a low volume fraction from 0.05% to 0.2% is recommended considering the homogeneity to ensure the evenly distribution of polypropylene fibers. Hence, a monofilament type of polypropylene fibers provided by Beijing Zhong Fang Technology (CTA) Co. Ltd (Fig.2) with an elongation rate between 15% and 35% were used in volume fraction of 0.05%, 0.1% and 0.15% with a diameter of 0.048mm, the lengths of the fibers used in the study were selected to be 8mm and 19mm, corresponding to aspect ratios of 167 and 396 respectively.

True triaxial facilities

The true triaxial testing system used was specially manufactured by the Science Academic Research Institute of Yangtze River in China. Fig.3 illustrates a schematic diagram of the apparatus. It accommodates a 150mmx150mmx150mm cubic specimen. Three directions of pressures were separately controlled by a servo-hydraulic system. It has a 1500tonne load capacity and is able to apply a lateral pressure of up to 20 MPa. Axial loads were applied to the specimen via actuators fitted at the bottom of the device and lateral loads were applied by actuators fitted against the device’s rigid reaction frame. All the pressures were measured by pressure transducers. Axial and lateral extensometers were used to measure the deformations caused by the imposed stresses.

Loading scheme

Under true triaxial compression, a displacement control with a 0.005mm/s loading velocity was applied in the axial direction (σ_3 direction) until ultimate failure occurred. This was done so that the entire stress-strain curve would include both ascending and descending branches. The lateral pressures ($\sigma_1 < \sigma_2$) were designated as 5/10 MPa, 4/15 MPa and 3/20 MPa respectively in accordance to the loading capacity of the testing machine. From the plasticity point of view, different lateral pressures lead to varying Lode angles such that a failure envelope with respect to the deviatoric tracing can be obtained. A load control was employed for the lateral pressure. Take the loading case of 5/10 MPa for example: the lateral pressures σ_1, σ_2 were initially imposed at a relatively low level (i.e., $\sigma_1 = \sigma_2 = 5$ MPa) with a loading velocity of about 0.8Mpa/s. Afterwards, σ_1 remained unchanged but σ_2 was increased to 10MPa. Consequently, axial displacement loading was utilized until ultimate failure occurred. The same loading scheme was also employed for the other two predetermined lateral pressures (4/15MPa and 3/20MPa).

Triaxial strength

Table 1 summarizes test results showing the axial strengths of plain concrete as well as HFRC subjected to true triaxial compression with predetermined lateral pressures of 5/10MPa, 4/15MPa and 3/20MPa. The listed triaxial strength for each loading scenario was the average value from three test specimens, of which the standard variation for each series was also given in the Table 1. The test results were then used to construct the failure surface of HFRC and calibrate the model's parameters (See section: Loading surface), and further detailed results with respect to the stress-strain behavior are elaborated in literature (Chi, 2012). As can be seen from Table 1 that by the inclusion of hybrid fibers, the triaxial strength increases up to 27.7% compared to the strength of plain concrete(C60). It is also observed that the enhancing effect of hybrid fiber is more significant rather than the effects caused by single steel and single polypropylene fiber.

Basic elastoplastic formulation

A basic assumption in the classical theory of incremental plasticity is that the total strain rate is divided into an elastic component $d\varepsilon_{ij}^{el}$ and a plastic component $d\varepsilon_{ij}^{pl}$ by simple superposition as shown here (Yu, 2006):

$$d\varepsilon_{ij}^{tot} = d\varepsilon_{ij}^{el} + d\varepsilon_{ij}^{pl} \tag{1}$$

At the beginning of loading, the behavior of FRC materials could be approximated as elastic, by virtue of all the deformations before initial yielding being recoverable after unloading. As a consequence, a Hooke's type stiffness matrix may be applied for calculating the elastic strain which involves two material constants when isotropy is assumed, namely, the elastic modulus E and the Poisson's ratio v, as expressed by this equation:

$$d\sigma_{ij} = D_{ijkl}^{el} \cdot d\varepsilon_{kl}^{el} = D_{ijkl}^{el} \cdot (d\varepsilon_{kl}^{tot} - d\varepsilon_{kl}^{pl}) \tag{2}$$

where $D_{ijkl}^{el} = 2G(\delta_{ik}\delta_{jl} + \frac{v}{1-2v}\delta_{ij}\delta_{kl})$ denotes the isotropic elastic tensor.

The elastic modulus generally rises with increasing steel fiber volume fraction and aspect ratio owing to the higher modulus of steel fiber. Likewise, it decreases as the polypropylene fiber volume fraction and aspect ratio increases because of polypropylene fiber's lower modulus. However, as a relatively low polypropylene fiber content is investigated in the research, and experimental observations (Zhang, 2010) indicate that it does not significantly influence elastic modulus E with various polypropylene fiber volume fractions ranging from 0% to 0.15%, its impact on the elastic stiffness of concrete thereof can be regarded as negligible. It is therefore assumed that the value of elastic modulus E has the following relationship with steel fiber volume fraction suggested by Huang (2004):

$$E = \frac{10^5}{2.2 + 34.74 / f_{fc}} \tag{3}$$

where f_{fc} represents the uniaxial compressive strength of SFRC, which can be calculated as:

$$f_{fc} = k_c \cdot f_{cu} \tag{4}$$

in which f_{cu} denotes the uniaxial compressive strength of plain concrete; the value of k_c will be addressed later.

In regards to the Poisson's ratio, the values most often quoted in the literature for FRC are in the range 0.2 to 0.25(ACI Committee 544,1996; Hu et al., 2003; Yin et al., 1989; Zhang et al., 2010). However, it was also reported that the average Poisson's ratio v remained practically unchanged regardless of the fiber type (Yin et al., 1989; Zhang, 2010) in the concrete, and according to the literature (ACI Committee 544), which referred that when the volume percentage of fibers is less than 2%, the Poisson's ratios of FRC are generally taken as equal to those of a similar non fibrous concrete. Consequently, a constant value of 0.2 is assumed for modeling of FRC in this study.

Moving forward, the plastic component $d\varepsilon_{ij}^{pl}$ is determined using plastic flow rule. Generally, a non-associated flow is assumed, which implies that the direction of the incremental plastic strain is normal to a plastic potential surface which differs from the loading surface and is given by:

$$d\varepsilon_{ij}^{pl} = d\lambda \frac{\partial g}{\partial \sigma_{ij}} \qquad (g \neq f) \tag{5}$$

where $d\lambda$ is the plastic multiplier determined in accordance to the consistency condition to ensure that the stress state after yielding satisfies the yield criteria at the end of each increment step.

Generally, the loading surface can be formulated in terms of either a combination of the three principal stress invariants or the coordinates in Haigh-Westergaard stress space (Fig.4) as expressed below:

$$f(\sigma_{ij}) = f(I_1, J_2, J_3) = f(\rho, \xi, \theta) = 0 \tag{6}$$

In this study, the loading surface comprises the three unified coordinates ρ, ξ, θ, which are computed as follows:

$$\xi = I_1 / \sqrt{3}, I_1 = tr\boldsymbol{\sigma} \tag{7}$$

$$\frac{\sigma_1}{f_c}, J_2 = (\mathbf{s}:\mathbf{s})/2 \tag{8}$$

$$\theta = \frac{1}{3}\cos^{-1}\left\{\frac{3\sqrt{3}}{2}\frac{J_3}{\sqrt{J_2^3}}\right\}, J_3 = \det(\mathbf{s}) \tag{9}$$

Loading surface

In this study, the mathematical form of the loading surface, involving the Willam-Warnke (W-W) five-parameter failure model is described using Haigh-Westergaard coordinates as follows:

$$f(\xi, \rho, \theta) = \sqrt{2J_2} - K(\bar{\varepsilon}_p)\cdot \rho^{hf}(\xi, \theta) = 0 \tag{10}$$

where $K_0 < K(\bar{\varepsilon}_p) \leq 1$ is the hardening/softening parameter that defines the increase of strength during hardening and the strength deterioration during softening. Before any plastic deformation occurs, the hardening parameter keeps a constant value of K_0, defining the initial yield surface that bounds the elastic region. The function $\rho^{hf}(\xi, \theta)$ defines the parabolic shape of meridians which bounds the ultimate strength of HFRC (Eq.13). It is interpolated between the tensile meridian ρ_t (Eq.11) where Lode angle $\theta = 0^\circ$, and the compressive meridian ρ_c (Eq.12) where Lode angle $\theta = 60^\circ$ as follows:

$$\frac{\xi}{f_{cu}} = a_2\left(\frac{k_t\rho_t}{f_{cu}}\right)^2 + a_1\left(\frac{k_t\rho_t}{f_{cu}}\right) + a_0 \tag{11}$$

$$\frac{\xi}{f_{cu}} = b_2\left(\frac{k_c\rho_c}{f_{cu}}\right)^2 + b_1\left(\frac{k_c\rho_c}{f_{cu}}\right) + b_0 \tag{12}$$

$$\rho^{hf}\left(\xi,\theta\right) = \frac{2\rho_c^{hf}[(\rho_c^{hf})^2 - (\rho_t^{hf})^2\cos\theta]}{4[(\rho_c^{hf})^2 - (\rho_t^{hf})^2]\cos^2\theta + (\rho_c^{hf} - 2\rho_t^{hf})^2} + \frac{\rho_c^{hf}(2\rho_t^{hf} - \rho_c^{hf})\{4[(\rho_c^{hf})^2 - (\rho_t^{hf})^2]\cos^2\theta + 5(\rho_t^{hf})^2 - 4\rho_t^{hf}\rho_c^{hf}\}^{1/2}}{4[(\rho_c^{hf})^2 - (\rho_t^{hf})^2]\cos^2\theta + (\rho_c^{hf} - 2\rho_t^{hf})^2} \tag{13}$$

in which $\rho_t^{hf} = k_t\rho_t, \rho_c^{hf} = k_c\rho_c$. $a_0, a_1, a_2, b_0, b_1, b_2$ are material constants sourced from a large number of typical experimental data points lying on the two meridians of conventional concrete. Because the tensile and compressive meridians intersect with the hydrostatic axis, they are subjected to equal triaxial tension which results in the parameter $a_0 = b_0$, thereby reducing the number of parameters to five, as shown below (Willam and Warnke, 1974):

$$\left.\begin{array}{l} a_0 = b_0 = 0.1775 \\ a_1 = -1.4554, a_2 = -0.1576 \\ b_1 = 0.7806, b_2 = -0.1763 \end{array}\right\} \tag{14}$$

It is also noted from Eq.10 to Eq.13 that apart from the concrete compressive strength (f_{cu}) which is a variable parameter, another two coefficients (k_c, k_t) are introduced into the meridian functions to account for the presence of hybrid fibers. These two coefficients can be calibrated from experimental results by considering the ultimate state of the failure surface, at which the value of hardening/softening function $K(\overline{\varepsilon}_p) = 1$.

Calibration of k_c

The coefficient k_c in Eq.12 for the compressive meridian of HFRC is determined by fitting the failure envelope to uniaxial compression test data to ensure that the compressive meridian passes through the HFRC's stress value at failure i.e. the uniaxial compressive strength of HFRC. Hereof, It has to be noted that because of the varying uniaxial compressive strength of HFRC, from the theory of plasticity point of view, the stress state $(\sigma_1, \sigma_2, \sigma_3) = (0, 0, -f_{fc})$ (compression is designated as negative) lying on the compressive meridian may lead to different hydrostatic stresses. The corresponding values of deviatoric stress ρ_c^{hf} and hydrostatic stress ξ can be calculated as:

$$\rho_c^{hf} = \sqrt{2 \cdot \frac{1}{6} \cdot \left[(0-0)^2 + (0+f_{fc})^2 + (-f_{fc}-0)^2 \right]} = \sqrt{\frac{2}{3}} \left| f_{fc} \right| \tag{15}$$

$$\xi = -f_{fc} / \sqrt{3} \tag{16}$$

By substituting the value of ξ into the W-W model, the deviatoric stress ρ_c on compressive meridian of plain concrete can then be determined as follows:

$$\rho_c = \frac{-b_1 - \sqrt{b_1^2 - 4b_2 (b_0 + \frac{1}{\sqrt{3}} \frac{f_{fc}}{f_{cu}})}}{2b_2} \cdot f_{cu} \tag{17}$$

the coefficient k_c is consequently determined by $k_c = \rho_c^{hf} / \rho_c$.

It is observed from the literature (Zhang, 2010) that the steel fiber has major influence on the compressive strength, whilst polypropylene fiber is reported to have no discernible effect on the compressive strength with relative low volume fractions ranging from 0.05% to 0.3% (Bayasi and Zeng, 1993) ,written as:

$$k_c = 1 + \alpha_{cu} \lambda_{sf} \tag{18}$$

where α_{cu} denotes the influence factor of steel fiber, it is fitted to 0.056 according to the experimental results reported in literature (Zhang, 2010). λ_{sf} denotes the FRI of steel fiber calculated as $\lambda_{sf} = V_{sf} \frac{l_{sf}}{d_{sf}}$, V_{sf} is the volume fraction of steel fiber and $\frac{l_{sf}}{d_{sf}}$ is the aspect ratio of steel fiber.

The calibrated values of k_c from the available experimental data reported in (Yin et al., 1989; Traina and Mansor, 1991; Chern et al., 1992; Lim and Navy, 2005; Jiao et al., 2007) which were not used in the calibration are also compared to Equation.18 as shown in Fig.5. It is clear that the value of k_c can be predicted for varying FRI by the approximate equation, and the predictions are in general agree with the test results reasonably well.

Calibration of k_t

As the points lying on the compressive meridians are first examined, the coefficient k_t in Eq.11 for the tensile meridian of HFRC is then calibrated by rotating the tensile meridian of plain concrete ρ_t and ensuring that the interpolated meridians as well as the deviatoric tracings coincide with all the test points under true triaxial compressions in this study as illustrated in Fig.6.

Subsequently, the value of k_t is determined according to the true triaxial test results calculated by $k_t = \rho_t^{hf} / \rho_t$, it is then regressed to the following equation by relating to FRI of both steel and polypropylene fiber:

$$k_t = 1 + 0.08\lambda_{sf} + 0.132\lambda_{pf} \tag{19}$$

where, λ_{pf} denotes the polypropylene fiber reinforcements index calculated as $\lambda_{pf} = V_{pf}\dfrac{l_{pf}}{d_{pf}}$, V_{pf} is the volume fraction of polypropylene fiber and $\dfrac{l_{pf}}{d_{pf}}$ is the aspect ratio of polypropylene fiber.

By using Eq.18 and Eq.19, the predicted values of deviatoric stresses $\rho^{hf}(\xi,\theta)$ are compared to the experimental results under all the lateral pressure combinations, as illustrated in Fig.7. It is seen that the proposed model is validated and provides fairly close estimation to the experimental values.

Hardening and softening functions

The hardening and softening rule define the shape and location of the loading surface as well as the material's response after initial yielding, wherein the hardening rule describes the pre-peak behavior as the elastic region terminates and the softening rule corresponds to the post-peak behavior during plastic flow. Generally, the evolution of subsequent surfaces is governed by a hardening/softening parameter which is usually related to the length of an accumulated plastic strain vector or an accumulated equivalent plastic strain (Chen, 1982). For the model in this study, the accumulated equivalent plastic strain is used as the hardening/softening parameter.

Isotropic hardening

Numerous experimental investigations carried out indicated that the loading envelope of concrete materials is similar to the shape of its failure envelope with the exception of the slight difference in the tension-tension zone (Tasuji et al, 1978). Therefore, an isotropic hardening (Chen 1988) is assumed in this study for simplicity, which indicates a uniform expansion of the loading surface, as shown in Fig.8. The hardening parameter is scaled by:

$$dk = d\bar{\varepsilon}_p \tag{20}$$

where k the hardening parameter is governed by the accumulated equivalent plastic strain $\bar{\varepsilon}_p$, of which the value is given as (Chen 1982):

$$d\bar{\varepsilon}_p = \int\sqrt{\frac{2}{3}d\varepsilon_{ij}^p d\varepsilon_{ij}^p} = \int d\lambda \cdot \|\mathbf{M}\| \tag{21}$$

where **M** denotes the gradient of the plastic potential such that $\mathbf{M} = \dfrac{\partial g}{\partial \sigma_{ij}}$.

The mathematical description of the hardening function involves an ascending part of Guo (1997) parabola:

$$K(k) = K(\bar{\varepsilon}_p) = \frac{\bar{\sigma}}{f_{cu}} = a\frac{\bar{\varepsilon}}{\varepsilon_c} + (3-2a)\left(\frac{\bar{\varepsilon}}{\varepsilon_c}\right)^2 + (a-2)\left(\frac{\bar{\varepsilon}}{\varepsilon_c}\right)^3 \tag{22}$$

For its numerical implementation, the hardening function is generalized as a rate form, given by:

$$dK(\bar{\varepsilon}_p) = \left[a\frac{1}{\varepsilon_c} + 2(3-2a)\left(\frac{\bar{\varepsilon}}{\varepsilon_c}\right)\frac{1}{\varepsilon_c} + 3(a-2)\left(\frac{\bar{\varepsilon}}{\varepsilon_c}\right)^2\frac{1}{\varepsilon_c}\right]\cdot d\bar{\varepsilon}_p = H_p(k,s)\cdot d\bar{\varepsilon}_p, \bar{\varepsilon} \le \varepsilon_c \tag{23}$$

where $\bar{\varepsilon}$ denotes the total equivalent strain at the current increment step, calculated with respect to a three-dimensional stress state (Yu, 2006):

$$\bar{\varepsilon} = \frac{1}{3}\left\{2\left[\left(\varepsilon_{xx}-\varepsilon_{yy}\right)^2+\left(\varepsilon_{yy}-\varepsilon_{zz}\right)^2+\left(\varepsilon_{xx}-\varepsilon_{zz}\right)^2\right]+3\left(\varepsilon_{xy}^2+\varepsilon_{yz}^2+\varepsilon_{zx}^2\right)\right\}^{\frac{1}{2}} \tag{24}$$

Coefficient a is a parameter related to the FRI of hybrid fibers which controls the slope of hardening curve to enable the hardening rule account for the presence of hybrid fibers. It was determined by Zhang (2010) through a uniaxial compression test as:

$$a = 28.2283 - 23.2771 f_{fc}^{\ 0.0374} + 0.4772\lambda_{sf} - 0.4917\lambda_{pf} \tag{25}$$

ε_c represents the amount of equivalent strain when the stress state reaches the failure surface. Here, for derivation of the ε_c of HFRC under true triaxial stresses, a linear relationship between a confinement level ($(\sigma_1+\sigma_2)/f_c$) and the strain amplification ($\varepsilon_c/\varepsilon_q$) under the true triaxial compression is developed, as shown in literature (Papanikolaou and Kappos, 2007), where ε_q the corresponding equivalent strain of HFRC at its uniaxial compressive strength is calculated as:

$$\varepsilon_q = \frac{2}{3}\left(\varepsilon_3 - \varepsilon_1\right) \tag{26}$$

the recommended value of ε_q is given according to literature (Zhang, 2010):

$$\varepsilon_q = 263.3\sqrt{f_{cu}(1+0.206\lambda_{sf}+0.388\lambda_{pf})}\times 10^{-6} \tag{27}$$

and the predictive equation for ε_c relating to the confinement level is then developed based on the true triaxial test results as:

$$\varepsilon_c = \varepsilon_q \cdot \left(1 + 20 \cdot \frac{\sigma_1+\sigma_2}{f_{cu}}\right) \tag{28}$$

where σ_1, σ_2 represent the applied lateral pressure respectively, which reduces to $\varepsilon_c = \varepsilon_q$ as subjected to the uniaxial compression. Fig.9 compares the predicted and experimental values of equivalent strain for HFRC for both the uniaxial (ε_q) and true triaxial compression loading cases (ε_c).

It was found during the testing that the strain of FRC material with various hybrid fiber combinations deviated significantly under different loadings, which is mainly attributed to the inherent discreteness of concrete material. Even though the approximations cannot always be mathematically consistent with the scattered experimental results, the proposed equations, as a reference, were still able to effectively characterize the peak strain of HFRC having different volume fractions and aspect ratios.

For equalbiaxial compression, the expression initially proposed by Darwin and Pecknold (1977) for plain concrete can be adopted and modified by using biaxial strength (f_{fcc})and uniaxial strength (f_{fc}) of FRC instead, written as:

$$\varepsilon_c = \varepsilon_q (3\frac{f_{fcc}}{f_{fc}} - 2) \tag{29}$$

Note that the softening contribution remains inactive during hardening process of numerical implementation.

Isotropic softening

For further plastic flow in post-peak regime, the value of hardening function is maintained as $K(k)=1$, at which point softening takes place and the material behavior is controlled by the softening function $K(s)$. This function governs the post-peak behavior of the loading surface i.e. when it contracts. A softening function, described in terms of the accumulated equivalent plastic strain and derived from the uniaxial compressive stress-strain relation was adopted. As the mathematical description of the softening function considered utilizes the descending part of the stress-strain equation proposed by Guo (1997):

$$K(s) = K(\bar{\varepsilon}_p) = \frac{\bar{\sigma}}{f_{cu}} = \frac{\dfrac{\bar{\varepsilon}}{\varepsilon_c}}{b\left(\dfrac{\bar{\varepsilon}}{\varepsilon_c} - 1\right)^2 + \dfrac{\bar{\varepsilon}}{\varepsilon_c}} \tag{30}$$

where $1 \geq K(s) > 0$.

For numerical implementation, the rate form of the softening function was generalized and differentiated as follows:

$$dK(\bar{\varepsilon}_p) = \frac{\frac{1}{\varepsilon_c}\left[b\left(\frac{\bar{\varepsilon}}{\varepsilon_c}-1\right)^2+\frac{\bar{\varepsilon}}{\varepsilon_c}\right]-\frac{\bar{\varepsilon}}{\varepsilon_c}\left[2b\left(\frac{\bar{\varepsilon}}{\varepsilon_c}-1\right)\frac{1}{\varepsilon_c}+\frac{1}{\varepsilon_c}\right]}{\left[b\left(\frac{\bar{\varepsilon}}{\varepsilon_c}-1\right)^2+\frac{\bar{\varepsilon}}{\varepsilon_c}\right]^2}\cdot d\bar{\varepsilon}_p = H_p(k,s)\cdot d\bar{\varepsilon}_p \, , \bar{\varepsilon} \geq \varepsilon_c \tag{31}$$

where ε_c is defined the same as with hardening regime(see Eq.28) and coefficient b, a parameter relating to the FRI of hybrid fibers, which controls the slope of the softening function was calibrated against the true triaxial experimental results to enable the softening rule simulate the varying softening behavior as the FRI changed. The b value was developed and computed using the following equation:

$$b = 0.01 + 0.037 f_{fc}^{\ 0.2846} - 0.02372\lambda_{sf} - 0.2335\lambda_{pf} \tag{32}$$

Consequently, at the end of each finite time interval $t_{n+1} = t_n + \Delta t$, the value of hardening/softening function is updated as:

$$K_{n+1} = K_n + dK_n(\bar{\varepsilon}_p) \tag{33}$$

Fig.10 shows the evolution of both hardening and softening regimes with respect to changing *a* and *b* values. It is worth noting that the proposed model is able to describe the various stress-strain behaviors that are usually arise as a result of varying fiber content.

Plastic potential

The plastic potential function plays a significant role in the correct estimation of the deformation capacity. It is the connection between the loading surface function and the stress-strain relation for a hardening material which determines the direction of plastic flow in terms of the gradient **M** (Eq.21). It is recognized from many literatures that associated flow assuming the direction of plastic strain increment normal to the loading surface restricts the inelastic volume dilatation or contraction behavior of concrete materials (Chen and Han, 1985), which results in a most conservative estimation of volumetric expansion. Hence in this study, a linear plastic potential of the Drucker-Prager model with a varying slope is adopted due to its simplicity:

$$g(\sigma_{ij},\alpha)=\alpha\xi+\rho-c=0 \tag{34}$$

where *c*= constant. Parameter α in above equation is the slope of the plastic potential function defined by the ratio:

$$\alpha=d\xi'/d\rho' \tag{35}$$

where $d\xi'$ denotes the first invariant of hydrostatic length and $d\rho'$ represents the second invariant of deviatoic length of plastic strain increment (see Imran, 1994). In this study, the Parameter α is assumed to be a constant during the loading for simplicity, calculated by $\alpha=\xi'/\rho'$, e.g. the hydrostatic part/deviatoric part of total plastic strain at peak stress.

Constitutive equations

In the elastic range, Hooke's elastic stiffness matrix ($\mathbf{D}^{el}$) associates the stress strain increments as follows:

$$d\boldsymbol{\sigma}=\mathbf{D}^{el}d\boldsymbol{\varepsilon}^{el}=\mathbf{D}^{el}(d\boldsymbol{\varepsilon}^{tot}-d\boldsymbol{\varepsilon}^{pl}) \tag{36}$$

where the plastic strain increment vector($d\boldsymbol{\varepsilon}^{pl}$) is evaluated via the plastic flow rule, it may be ascribed to either the associate plastic potential or the non-associated plastic potential, written as shown:

$$d\boldsymbol{\varepsilon}^{pl}=d\lambda\frac{\partial f}{\partial\boldsymbol{\sigma}} \text{ or } d\boldsymbol{\varepsilon}^{pl}=d\lambda\frac{\partial g}{\partial\boldsymbol{\sigma}} \tag{37}$$

wherein the plastic multiplier(λ) is determined using the consistency condition, implying that:

$$df = \frac{\partial f}{\partial \boldsymbol{\sigma}} d\boldsymbol{\sigma} + \frac{\partial f}{\partial K}\frac{\partial K}{\partial \boldsymbol{\varepsilon}^{pl}} d\boldsymbol{\varepsilon}^{pl} = 0 \tag{38}$$

and where the hardening parameter K is a function of accumulated plastic strain in this study. $d\lambda$ is then solved as:

$$d\lambda = \frac{(\partial f / \partial \boldsymbol{\sigma})\mathbf{D}^{el} d\boldsymbol{\varepsilon}^{tot}}{\frac{\partial f}{\partial \boldsymbol{\sigma}}\mathbf{D}^{el}\frac{\partial g}{\partial \boldsymbol{\sigma}} - \frac{\partial f}{\partial K}\frac{\partial K}{\partial \boldsymbol{\varepsilon}^{pl}}\frac{\partial g}{\partial \boldsymbol{\sigma}}} \tag{39}$$

By substituting of Eq.39 and Eq.37 into Eq.36 and solving for $d\boldsymbol{\sigma}$, we obtain:

$$d\boldsymbol{\sigma} = \left(\mathbf{D}^{el} - \frac{\mathbf{D}^{el}\frac{\partial g}{\partial \boldsymbol{\sigma}}\frac{\partial f}{\partial \boldsymbol{\sigma}}^{T}\mathbf{D}^{el}}{\frac{\partial f}{\partial \boldsymbol{\sigma}}\mathbf{D}^{el}\frac{\partial g}{\partial \boldsymbol{\sigma}} - \frac{\partial f}{\partial K}\frac{\partial K}{\partial \boldsymbol{\varepsilon}^{pl}}\frac{\partial g}{\partial \boldsymbol{\sigma}}} \right) d\boldsymbol{\varepsilon}^{tot} \tag{40}$$

The elastoplastic matrix $\mathbf{D}^{ep}$ may then be expressed as:

$$\mathbf{D}^{ep} = \mathbf{D}^{el} - \mathbf{D}^{pl} \tag{41}$$

where $\mathbf{D}^{pl}$ denotes the plastic stiffness matrix representing stiffness degradation as a results of the plastic flow.

Validations

An iteration algorithm, which was originally proposed by Sloan (1987), is developed for the numerical integration of elastoplastic stress-strain relations of HFRC (Chi, 2012). This scheme was then specifically incorporated into ABAQUS through a User-defined Material subroutine (UMAT). Apart from the proposed constitutive model, the development of an appropriate and separate finite element model was undertaken in this study. In view of the loading situation in true triaxial compression with no bending moment and bending deformation of the specimen observed, a 'C3D8' element, which is an iso-parametric, eight-noded solid element, was selected for the numerical simulation, and Fig.11 illustrates the finite element mesh. The size of the finite element model used exactly matched that of the tested specimen, and the lateral pressure applied was the same as in the true triaxial test. Additionally, the FE model used strain control for vertical loading to capture the post peak behavior of the FRC.

The model's response was initially validated by comparing its outputs with results from the true triaxial test. Fig 12 shows a representative comparison of the analytical and the experimental results of HFRC under true triaxial compression with a lateral pressure combination of 4/15MPa. The input parameters were calibrated using respective equations described in previous sections. It is observed that the proposed model provides a fairly good estimate of ultimate stresses, whereas the strains in lateral direction showed a moderate deviation. The discrepancies observed between the analytical and experimental results assessed were largely stemming from the difference between the scattered experimental results and developed equations (see Fig.9).

Verifications

failure envelope

The failure model was compared to the strengths of FRC as determined by earlier existing multiaxial tests. In the ρ- ξ plane, the experimental results of Chern et al.(1992) were compared to the developed model's outputs as shown in Fig.13. For the triaxial strength of SFRC, the data points falling on the compressive and tensile meridians were compared to the proposed model, in which the volume fractions of steel fiber ranged from 0% to 2% for a fixed aspect ratio of 44. Good correlation was observed for relatively low hydrostatic pressures (ξ/f_c <5), while the predicted strengths appear to be slightly underestimated for higher hydrostatic pressures (ξ/f_c >5).

Fig.14 shows the comparison between the proposed model's envelope and the experimental data of SFRC as provided by Song et al. (1994) in the deviatoric plane. Song et al., (1994) conducted their tests under true triaxial loading for different Lode angles, shown lying on the interpolated meridians in Fig.14. Typical data points representing to different Lode angles and hydrostatic pressures were selected for the comparison, wherein the steel fiber volume fraction was fixed at 1%, having an aspect ratio of 50. It is evident that the proposed model's envelope gives a close approximation of the experimental data point for the various Lode angles and hydrostatic pressures considered.

Furthermore, the proposed model's biaxial failure envelope was verified using experimentally derived data points of SFRC under varying biaxial loading ratio as illustrated in Figs.15 and 16. In Fig.15, the data points determined by Traina et al.(1991) were compared to the proposed model's biaxial envelopes, wherein the steel fiber volume fraction ranges from 0% to 1.5%, having a fixed aspect ratio of 60. In addition, Yin et al's., (1989) test results were also used for the verification, having steel fibers aspect ratios of 45 and 59, as shown in Fig.16.

It is seen from the above figures that although the predicted strengths may not always coincide with the scattered experimental data points, the proposed model's failure envelope is still be able to predict with reasonable accuracy the ultimate strengths of fiber reinforced concrete having different volume fractions and aspect ratios, and subjected to multiaxial loading.

stress-strain curves

The numerical performance of the developed constitutive model was evaluated by comparing its outputs against multiaxial stress-strain relations. Prior to comparing the experimental results, it must be noted that all the relevant input parameters in each experimental study were calibrated before numerical analysis commenced, where the parameters k_c, k_t , a, b and ε_c are calibrated using Eqs.18, 19, 25, 32 and 28, 29 respectively.

Figs.17 and 18 compare the analytical results to the experimental results of plain concrete under uniaxial compression as determined by Kupfer et al., (1969) and plain concrete under laterally confined triaxial compression provided by Kotsovos et al., (1978) in both axial and lateral directions. In Kupfer et al., (1969), $f_{cu} = 32.1$ MPa, $E = 2.9 \times e^4$ MPa, and model parameters were calibrated to *a*=1.727, *b*=0.109, *kc*=*kt*=1, $\varepsilon_c = 0.00149$. In Kotsovos et al., (1978), $f_{cu} = 31.7$ MPa, $E = 3 \times e^4$ MPa and the model parameters were set to $a = 1.739, b = 0.109, k_c = k_t = 1$, and $\varepsilon_c = 0.03702$ for laterally confined triaxial compression (σ_1=σ_2=-19MPa), $\varepsilon_c = 0.04638$ and $\varepsilon_c = 0.08379$ for (σ1=σ2=-24MPa) and (σ1=σ2=-44MPa) respectively. It is seen that the stress-strain behaviors of plain concrete are well predicted by the constitutive model. It can therefore be inferred that the developed model will revert back to the behavior of plain concrete with the removal of the fibers.

Fig.19 shows the comparison between the predicted curves and experimental results of HFRC (with steel fiber volume fraction ranging from 0.5% to 1.5% and aspect ratio of 30, and polypropylene fiber at 0.1% fixed volume fraction and aspect ratio of 167) under uniaxial compression as reported by Zhang (2010). Based on Zhang's test with $f_{cu} = 28.6$ MPa and $E = 2.9 \times e^4$ MPa, the model parameters were calibrated as shown below: *a*=1.83, *b*=0.064, *kc*=1.0084, *kt*=1.034, $\varepsilon_c = 0.00147$ (for SA05PA10), *a*=1.902, *b*=0.06, *kc*=1.0168, *kt*=1.046, $\varepsilon_c = 0.00149$ (for SA10PA10), *a*=1.974, *b*=0.056, *kc*=1.0252, *kt*=1.058, $\varepsilon_c = 0.00151$ (for SA15PA10). As shown in Fig.19, very good conformance exists between the experimental and analytical curves of HFRC where both strength and deformation is concerned, with the exception of a slight underestimation of strength loss at the latter stages of the softening period.

Moving forward, the constitutive models description of equal biaxial stress-strain behavior of SFRC was experimentally derived from results (Traina et al., 1991) that utilized SFRC (with steel fiber volume fraction of 0.5% and aspect ratio of 33) as shown in Fig.20. Similarly Yin et al's (1989) results were compared to the model's output for steel fiber volume fraction of 1% with aspect ratio of 45 as shown in Fig.21. In Traina et al. (1991), $f_{cu} = 40$ MPa, $E = 3.2 \times e^4$ MPa and the model parameters are calibrated to $a = 1.586, b = 0.112, k_c = 1.0092, k_t = 1.013, \varepsilon_c = 0.00196$. In Yin et al. (1989), $f_{cu} = 37.6$ MPa, $E = 3.2 \times e^4$ MPa, and the model parameters are set as $a = 1.784, b = 0.103, k_c = 1.0252, k_t = 1.036, \varepsilon_c = 0.00195$.

It is noted from Figs.20 and 21 that the analytical results yield a slightly conservative estimation of the biaxial strength of SFRC, whilst both the axial and lateral strains are in good concurrence with the experimental values. Moreover, due to the absence of softening curves in Traina et al., (1991) and Yin et al., (1989), the predicted curve in post-peak region may prove useful as a reference for further comparison.

Finally, typical experimental results of SFRC obtained by Chern et al. (1992) under triaxial compression were compared to the model's prediction. Fig.22 shows the triaxial stress-strain behavior of SFRC with 2% steel fiber volume fraction and aspect ratio of 44 in both axial and lateral directions. The concrete specimens were subjected to lateral confining pressures ranging from 10MPa up to 70MPa. In this comparison, $f_{cu} = 20.65$ MPa, $E = 2.6 \times e^4$ MPa, the model parameters are set to $a = 2.85, b = 0.077, k_c = 1.0493, k_t = 1.07$, and $\varepsilon_c = 0.02649$ for 10MPa confining pressure, $\varepsilon_c = 0.05168$ for 20MPa, $\varepsilon_c = 0.10206$ for 40MPa and $\varepsilon_c = 0.17763$ for 70MPa respectively.

As shown in Fig.22, the proposed model provides a good estimation of triaxial strength for relative low confinement (<40MPa), however, the predicted ductility performance due to the lateral confinement is underestimated. In addition, the axial strength appears to be underestimated for increasing confinement levels, in that it deviates by about 10% from the experimental value as the lateral confining pressure reaches 70MPa. However from a safety point of view, the proposed model is reliable and mostly yields conservative estimations.

In general, Figs.17 to 22 have shown that, the proposed constitutive model covers a wide range of experimental data with its output reproducing the majority of the experimental stress-strain curves evaluated within reasonable accuracy. The model has also been shown to be capable of describing the important characteristics of FRC behavior. It is believed from the comparisons made that the proposed constitutive model is adequate to be applied in the numerical simulation of fiber reinforced concrete materials.

Conclusion

A plasticity theory based constitutive model for HFRC material under true triaxial compression was developed in this study. It incorporates a five-parameter Willam-Warnke type failure surface as well as the uncoupled isotropic hardening and softening regimes determined using accumulated equivalent plastic strain and the non-associated flow rule in conjunction with a linear Drucker-Prager type plastic potential function.

Two coefficients relating to the FRI and introduced into the meridian functions to account for the presence of hybrid fibers were calibrated using experimental results of this study. It was demonstrated that the prediction of deviatoric stresses provides a close estimation of the experimental values with small discrepancy. In addition, it was shown that the proposed failure envelope could also be recovered and applied in the prediction of the multiaxial strength of conventional concrete without fiber reinforcement.

The proposed hardening and softening rules were found to be the source of the stiffness changes in the pre-peak region as well as the different ductile performances induced by hybrid fiber in the post-peak region. A linear relationship between confinement level and strain amplification under multiaxial loading was also proposed in the hardening and softening function, for which the approximation derived correlated reasonably well with the scattered experimental results.

The response of the proposed constitutive model was verified against existing experimental results reported by various researchers. It was deduced from the results that the developed model would revert back to a model of plain concrete with the removal of the fiber component. It was also determined that the proposed model's failure envelope provides accurate approximations of ultimate strength for both plain concrete and fiber reinforced concrete under various loading situations.

Acknowledgement

The author is grateful to the support granted by CSC funding. This study reported is a part of the NSFC project (No. 51078295). Sincere thanks are due to all the valuable comments and suggestions given by the reviewers which have contributed to a significant improvement of our paper.

References

ACI Committee 544., 1982. State-of-the-Art Report on Fiber Reinforced Concrete. ACI 544.1R-82, American Concrete Institute, Detroi, 16pp.

ACI Committee 544., 1996. Report on Fiber Reinforced Concrete. ACI 544.1R-96, American Concrete Institute, Detroi, 64pp.

Ansari,F., Li,Q., 1998. High-Strength Concrete Subjected to Triaxial Compression. ACI Materials Journal 95(6), 747-755.

Attard, M.M., Setunge, S., 1996. Stress-strain relationship of confined and unconfined concrete. ACI Materials Journal 93, 432-442.

Babu, R.R., Gurmail, S. B., Arbind, K.S., 2006. Plasticity-based constitutive model for concrete in stress space. Latin American Journal of Solids and Structures 3, 417-441.

Bayasi, Z., Zeng, J., 1993. Properties of Polypropylene fiber reinforced concrete. ACI Material Journal 90(6), 605-610.

Belarbi, A., Hsu,T.T.C., 1995. Constitutive Laws of Softened Concrete in Biaxial Tension Compression. ACI Structural Journal 92(5), 562-573.

Bentur, A., Mindess, S., 1990. Fiber Reinforced Cementitious Composites, Elsevier Applied Science., London.

Candappa, D. C., Sanjayan, J. G., Setunge, S., 2001. Complete triaxial stress-strain curves of high-strength concrete. Journal of Materials in Civil Engineering 13(3), 209–215.

Chen, W.F., 1982. Plasticity in reinforced concrete. McGraw-Hill Book LTD, New York.

Chen, W.F., Han, D.J., 1988. Plasticity for Structural Engineers. Springer-Verlag Inc., New York.

Chern, J. C., Yang, H. J., Chen, H. W., 1992. Behavior of Steel Fiber Reinforced Concrete in Multiaxial Loading. ACI Materials Journal 89(1), 32-40.

Chi, Y., 2012. Plasticity Theory Based Constitutive Modelling of Hybrid Fibre Reinforced Concrete. Ph.D thesis, the University of Nottingham, Nottingham, UK.

China standardization., 2002. Test Method for Mechanical Performance of Plain Concrete (GB/T50081-2002). China Building Industry Press, China

Chinn, J., Zimmerman, R. M., 1965. Behavior of Plain Concrete under Various High Triaxial Compression Loading Conditions, Technical Report No. WL TR 64-163, Air Force Weapons Laboratory, 146pp.

Darwin, D., Pecknold, D.A., 1977. Nonlinear biaxial stress-strain law for concrete. Journal of Engineering Mechanics 103(2), 229-241.

Grassl, P., Lundgren, K., Gylltoft, K., 2002. Concrete in compression: a plasticity theory with a novel hardening law. International Journal of Solids and Structures 39(20), 5205–5223.

Guo, Z. H., 1997. The strength and deformation of concrete—experimental results and constitutive relationship, Tsinghua University Press, Beijing.

Hsu, L.H., Hsu, C.T.T., 1994. Stress-Strain Behavior of Steel-Fiber High-Strength Concrete under Compression. ACI Structural Journal 91(4), 448-457.

Hu, X.D., Day, R., Dux, P., 2003. Biaxial Failure Model for Fiber Reinforced Concrete. Journal of Materials in Civil Engineering 15(6), 609-615.

Huang, C.K., 2004. Structure of Fiber Reinforced Concrete. China Machine Press., Beijing.

Hussein, A., Marzouk, H., 2000. Behavior of high-strength concrete under biaxial stresses. ACI Materials Journal 97(1), 27–36.

Imran, I., Pantazopoulou, S. J., 1996. Experimental Study of Plain Concrete under Triaxial Stress. ACI Materials Journal 93(6), 589-601.

Imran, I., Pantazopoulou, S.J., 2001. Plasticity model for concrete under triaxial compression. Journal of Engineering Mechanics 127(3), 281-290.

Jiao, C.J, Zhan, Z.F., 2007. Experimental study of hybrid fiber reinforced concrete under compression. Journal of Guangzhou University(Natural Science Edition) 6(4),70-73.

Kotsovos, M.D., Newman, J.B., 1999. Generalized stress-strain relations for concrete. Journal of Engineering Mechanics125(8), 845-856.

Kupfer, H., Hilsdorf, H. K., Rusch, H., 1969. Behavior of Concrete under Biaxial Stresses. ACI Journal Proceedings 66(8), 656-666.

Lim, D.H., Nawy, E.G., 2005. Behaviour of plain and steel-fiber-reinforced high-strength concrete under uniaxial and biaxial compression. Magazine of concrete research 57(10), 603-610.

Lu, X., Hsu, C.T.T., 2006. Behavior of high strength concrete with and without steel fiber reinforcement in triaxial compression. Cement and Concrete Research 36 , 1679–1685.

Murugappan, K., Paramasivam, P., Tan, K. H., 1993. Failure envelope for steel fiber concrete under biaxial compression. Journal of Materials in Civil Engineering 5(4), 436-446.

Nataraja, M. C., Dhang, N., Gupta, A. P., 1999. Stress strain curve for steel-fiber reinforced concrete under compression. Cement and Concrete Composite 21, 383–390.

Papanikolaou, V.K., Kappos, A.J., 2007. Confinement-sensitive plasticity constitutive model for concrete in triaxial compression. International Journal of Solids and Structures 44, 7021-7048.

Prisco, M.D., Plizzari, G., Vandewalle, L., 2009. Fiber reinforced concrete: new design perspectives.

Materials and Structures 42, 1261-1281.

Seow, P.E.C., Swaddiwudhipong, S., 2005. Failure surface for plain concrete and SFRC under multi-axial loads—a unified approach. Journal of Materials in Civil Engineering 17(2), 219–228.

Sloan, S.W., 1987. Substepping schemes for the numerical integration of elastoplastic stress-strain relations. International journal for numerical methods in engineering. 24, 893-911.

Swamy, R. N., Barr, B., 1989. Fiber reinforced cements and concretes: recent developments. Elservier Science Publisher LTD, New York.

Tasuji, I., Slate, F., Nilson, A., 1978. Stress-Strain Response and Fracture of Concrete in Biaxial Loading. ACI Journal Proceedings 75(7), 306-312.

Traina, L. A., Mansour, S. A., 1991. Biaxial strength and deformational behavior of plain and steel fiber concrete. ACI Materials Journal 88(4), 354-362.

William, K. J., Warnke, E. P., 1974. Constitutive model for the triaxial behaviour of concrete (paper III-l). Seminar on Concr. Struct. Subjected to Triaxial Stresses, Int. Assoc, of Bridge and Struct. Engrg.

Yin, W., Su, E., Mansour, M., Hsu, T., 1989. Biaxial Tests of Plain and Fiber Concrete. ACI Materials Journal 86(3), 236-243.

Yu, H.S. 2006. Plasticity and geotechnics., Springer.

Yun, H.D., Yang, I.S., Kim, S.W., 2007. Mechanical properties of high-performance hybrid-fiber reinforced cementitious composites(HPHFRCCs). Magazine of Concrete Research 59(4), 257-271.

Zhang, Y., 2010. Study on Uniaxial Compressive Constitutive Relationship and Uniaxial Tensile Behavior of Steel-Polypropylene Hybrid Fiber Reinforced Concrete. Ph.D thesis, Wuhan University, Wuhan, China.

Table 1.Strengths of HFRC under true triaxial compressions

No.	Specimen Number	Volume fraction of SF /%	Volume fraction of PF /%	Aspect ratio of SF	Aspect ratio of PF	$\overline{x}$ for 5/10 (MPa)	SV 5/10 (MPa)	$\overline{x}$ for 4/15 (MPa)	SV 4/15 (MPa)	$\overline{x}$ for 3/20 (MPa)	SV 3/20 (MPa)
1	SA05PA05	0.5	0.05	30	167	106.6	2.4	110.8	6.3	115.5	7.2
2	SA05PB05	0.5	0.05	30	396	109.1	3.5	111.4	2.5	115.5	8.4
3	SB05PA05	0.5	0.05	60	167	115.2	2.5	115.3	8.1	117.3	6.9
4	SB05PB05	0.5	0.05	60	396	108.7	5.8	113.2	0.5	119.8	7.4
5	SA05PA10	0.5	0.10	30	167	107.2	3.9	109.5	2.9	112.3	7.1
6	SA05PA15	0.5	0.15	30	167	109.1	0.9	112.1	1.5	120.8	2.1
7	SA10PA05	1.0	0.05	30	167	111.3	4.9	113.3	1.4	118.0	3.5
8	SA10PA10	1.0	0.10	30	167	109.2	2.2	108.9	4.5	118.1	3.7
9	SA10PB10	1.0	0.10	30	396	109.7	1.6	112.5	7.1	112.9	0.4
10	SB10PA10	1.0	0.10	60	167	113.5	0.6	123.7	6.4	126.2	7.9
11	SB10PB10	1.0	0.10	60	396	115.2	2.4	116.5	0.7	125.0	6.2
12	SA10PA15	1.0	0.15	30	167	115.7	5.8	115.7	2.2	128.5	1.2
13	SA15PA05	1.5	0.05	30	167	115.3	0.1	122.4	3.1	121.8	1.4
14	SA15PA10	1.5	0.10	30	167	118.7	2.3	126.4	5.5	129.1	3.3
15	SA15PA15	1.5	0.15	30	167	115.7	0.6	126.7	6	134.0	4
16	SA15PB15	1.5	0.15	30	396	120.8	1.2	123.7	7.1	123.3	1.7
17	SB15PA15	1.5	0.15	60	167	119.4	2	124.9	14	133.4	9.1
18	SB15PB15	1.5	0.15	60	396	118.5	0.2	118.3	8.1	125.4	3.9
19	SA05	0.5	-	30	-	107.6	5.6	111.4	7.1	114.7	3.8
20	SA10	1.0	-	30	-	108.9	7.6	116.0	5	119.7	2.5
21	SA15	1.5	-	30	-	124.2	2.3	121.3	3.9	130.6	4.5
22	PA05	-	0.05	-	167	101.5	4.4	110.8	7.6	114.9	3.2
23	PA10	-	0.10	-	167	106.2	3.7	106.7	4.1	111.7	3.3
24	PA15	-	0.15	-	167	103.8	6.5	104.4	5	112.9	5.1
25	C60	-	-	-	-	102.0	2.9	101.7	2.5	104.5	2.5

Remarks: SV denotes the standard variation, which is calculated by $\sqrt{\sum\frac{\left(x-\overline{x}\right)^2}{n-1}}$, where n=3 represents the number of specimens tested for each loading scenario. $\overline{x}$ represents the average value of the tested triaxial strengths.

Figure 1
Click here to download Figure: Fig 1.pdf

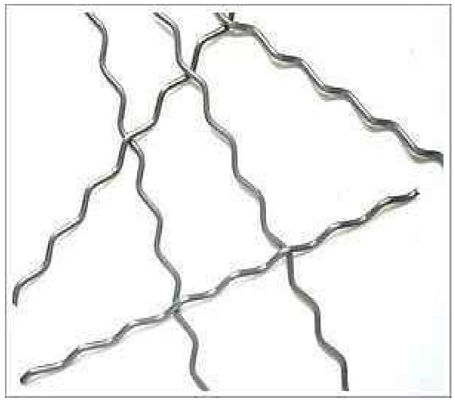

Fig.1 Steel fiber

Figure 2
Click here to download Figure: Fig 2.pdf

Fig.2 CTA Polypropylene fiber

Figure 3
Click here to download Figure: Fig 3.pdf

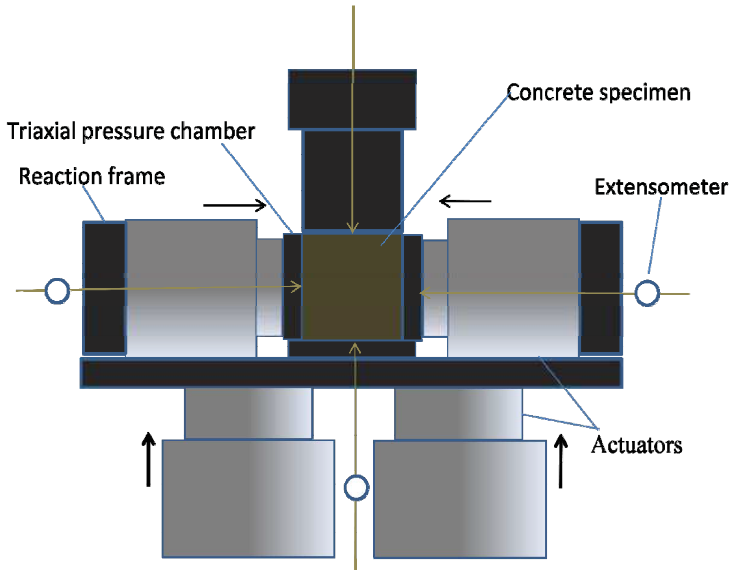

Fig.3 Schematic diagram of testing system

Figure 4
Click here to download Figure: Fig 4.pdf

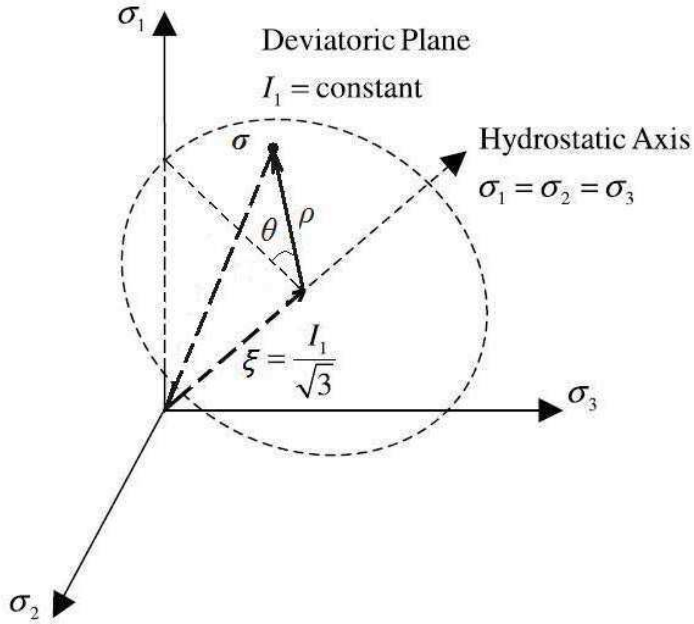

Fig.4 Stress invariants in the Haigh-Westergaard stress space

Figure 5
Click here to download Figure: Fig 5.pdf

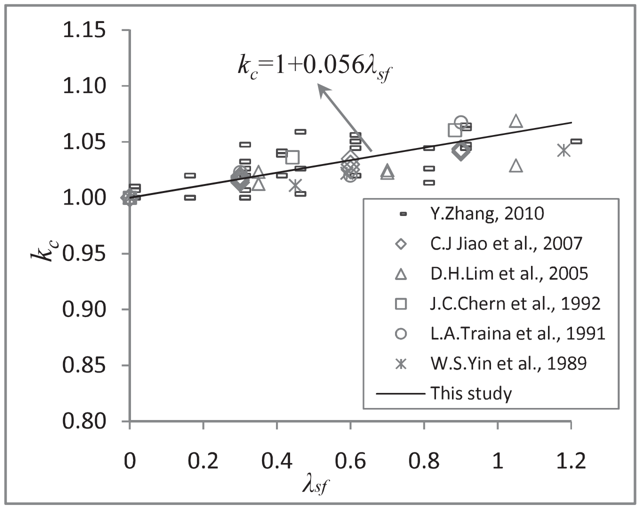

Fig.5 Comparison of coefficient k_c with previous experimental results

Figure 6
Click here to download Figure: Fig 6.pdf

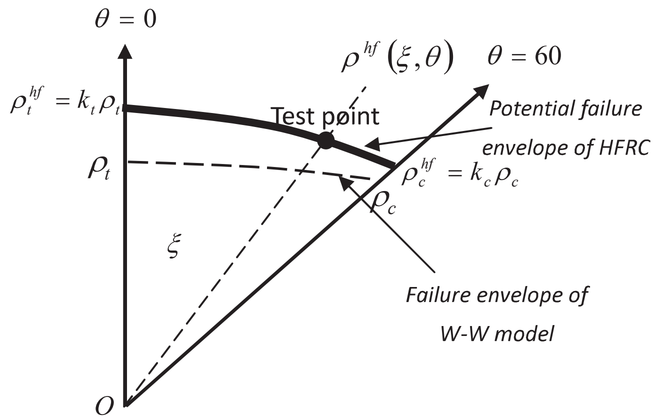

Fig.6 Approach to examine the value of coefficient k_t

Figure 7
Click here to download Figure: Fig 7.pdf

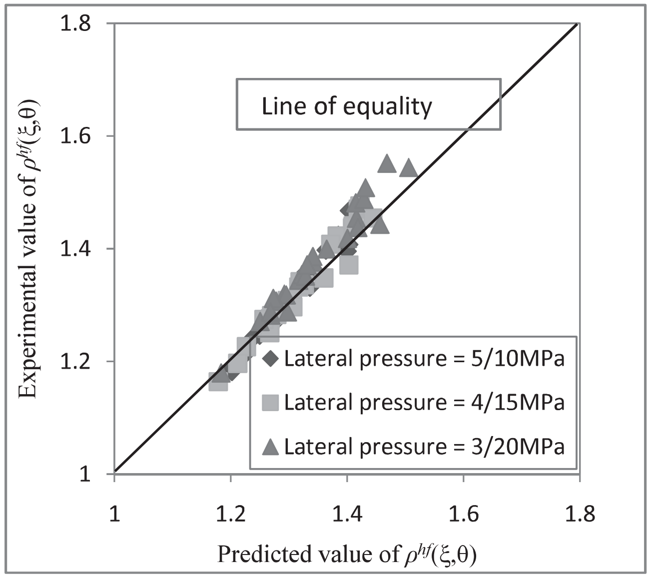

Fig.7 Comparisons of deviatoric stresses between experimental and analytical results

Figure 8

Click here to download Figure: Fig 8.pdf

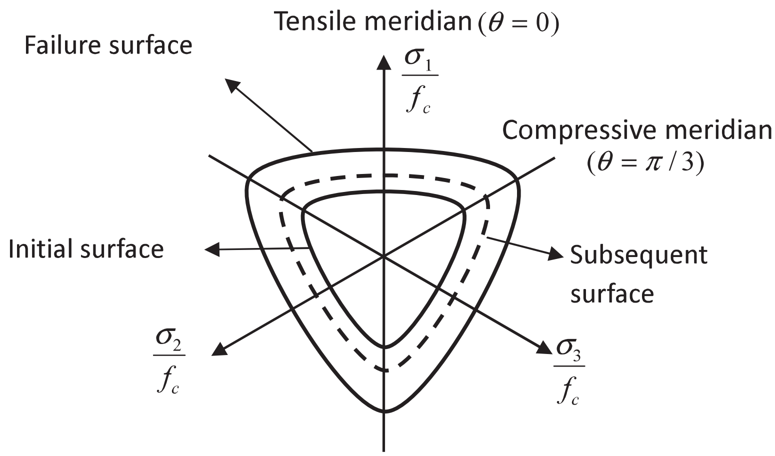

Fig.8 Isotropic hardening in deviatoric plane

Figure 9a

Click here to download Figure: Fig 9a.pdf

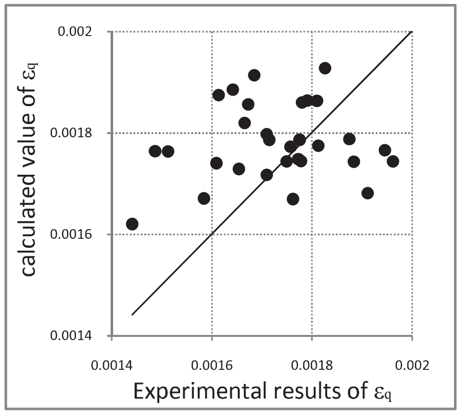

(a)

Fig.9 comparison between tested value and approximation of ε_q in uniaxial (a) as well as that of ε_c in true triaxial loading case (b)

Figure 9b

Click here to download Figure: Fig 9b.pdf

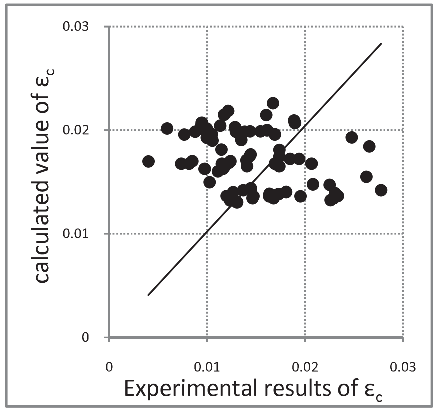

(b)

Fig.9 comparison between tested value and approximation of ε_q in uniaxial (a) as well as that of ε_c in true triaxial loading case (b)

Figure 10
Click here to download Figure: Fig 10.pdf

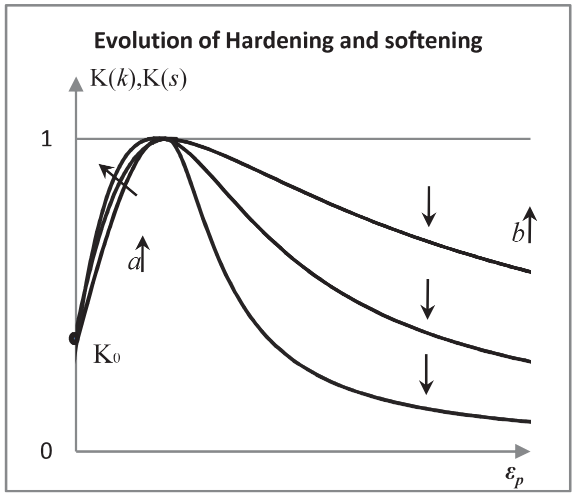

Fig.10 Uncoupled hardening and softening regime

Figure 11
Click here to download Figure: Fig 11.pdf

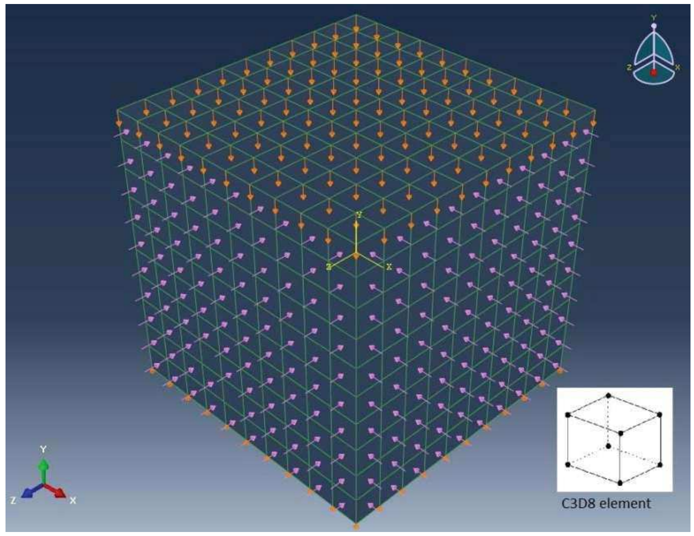

Fig.11 Finite element mesh with C3D8 elements

Figure 12
Click here to download Figure: Fig 12.pdf

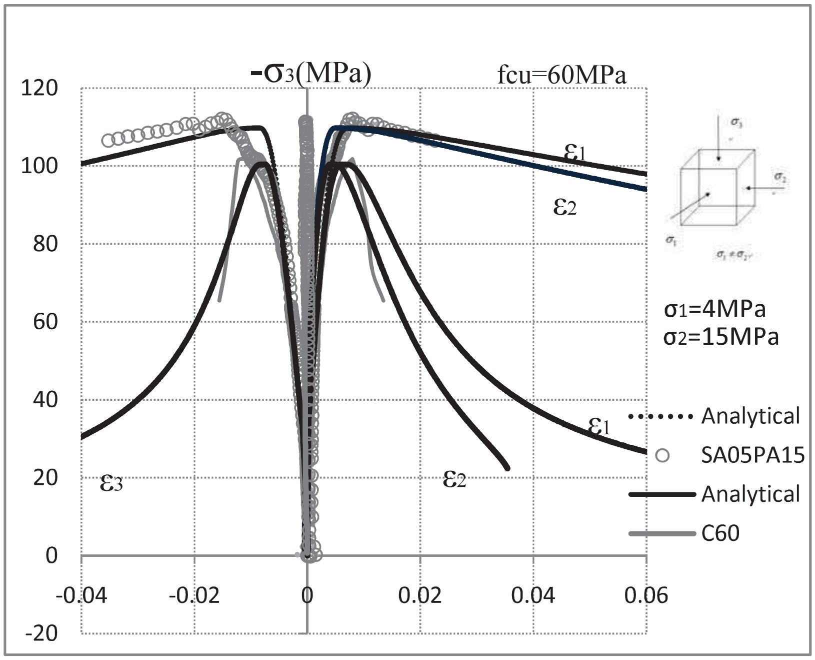

Fig.12 Comparison between analytical and the experimental stress-strain relations under a lateral pressure combination of 4/15MPa

Figure 13
Click here to download Figure: Fig 13.pdf

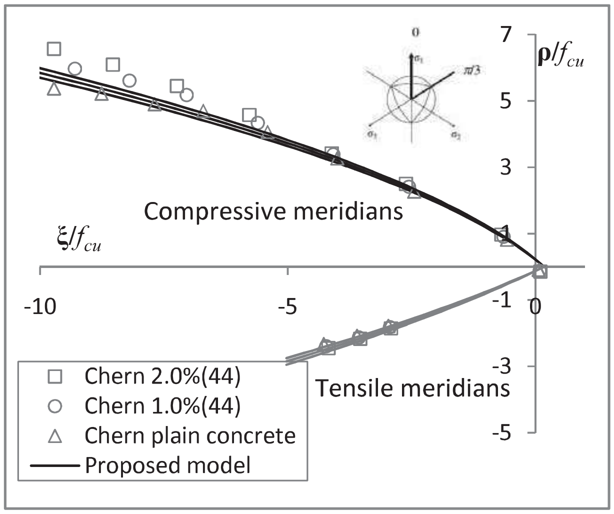

Fig.13 Comparison between meridians of proposed model and experimental data (of Chern et al., 1992)

Figure 14
Click here to download Figure: Fig 14.pdf

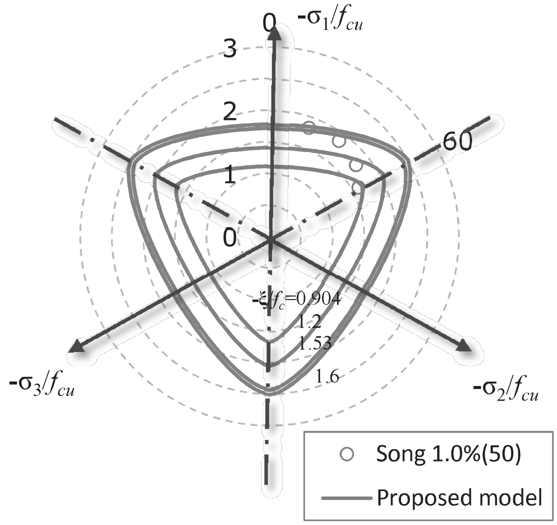

Fig.14 Comparison between deviatoric tracings of proposed model and experimental data (of Song et al., 1994)

Figure 15
Click here to download Figure: Fig 15.pdf

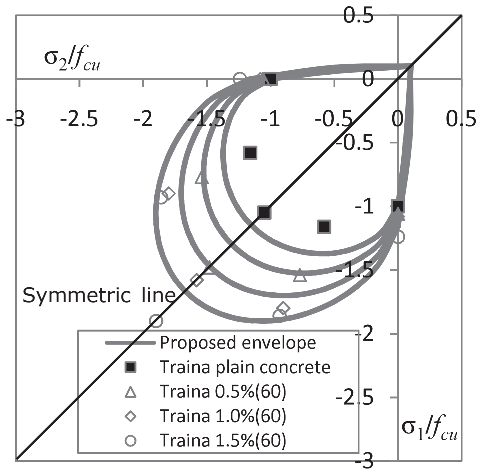

Fig.15 Comparison with Traina et al.(1991)

Figure 16
Click here to download Figure: Fig 16.pdf

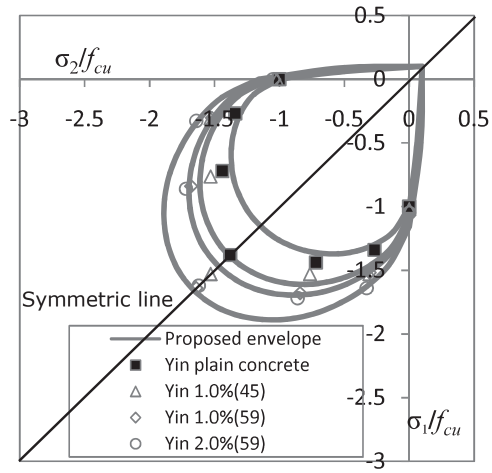

Fig.16 Comparison with Yin et al.(1989)

Figure 17
Click here to download Figure: Fig 17.pdf

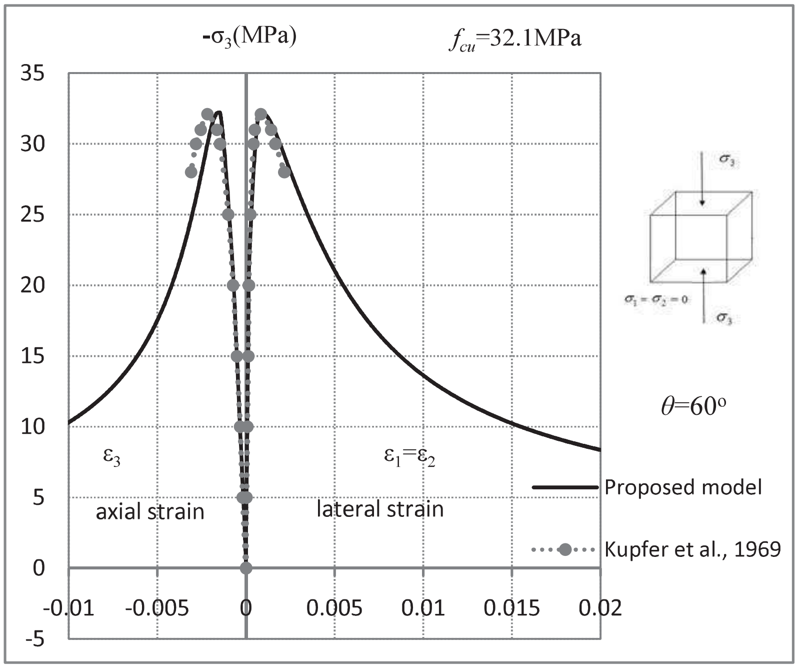

Fig.17 Comparison with Kupfer et al., (1969)

Figure 18
Click here to download Figure: Fig 18.pdf

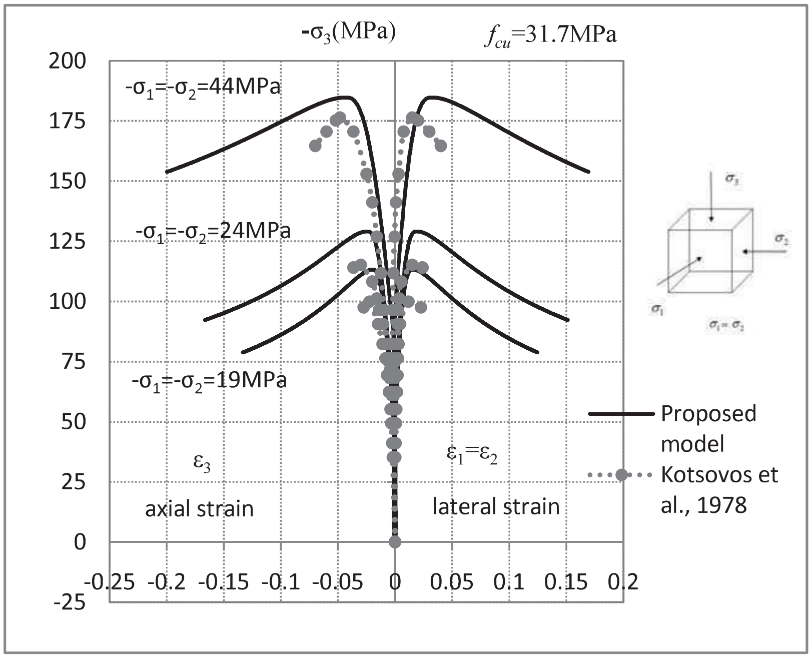

Fig.18 Comparison with Kotsovos et al.,(1978)

Figure 19
Click here to download Figure: Fig 19.pdf

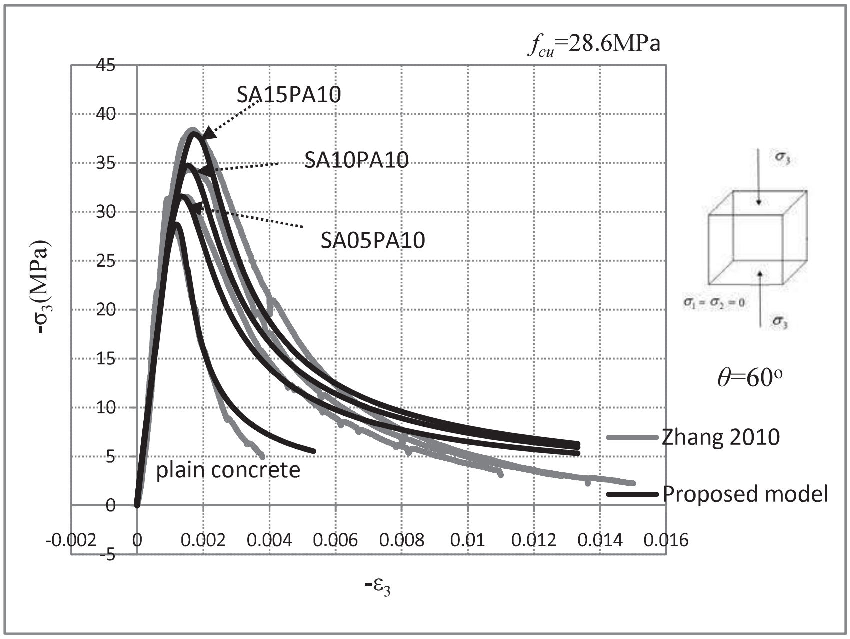

Fig.19 Comparison of uniaxial stress-strain relation of HFRC between analytical and experimental

Figure 20
Click here to download Figure: Fig 20.pdf

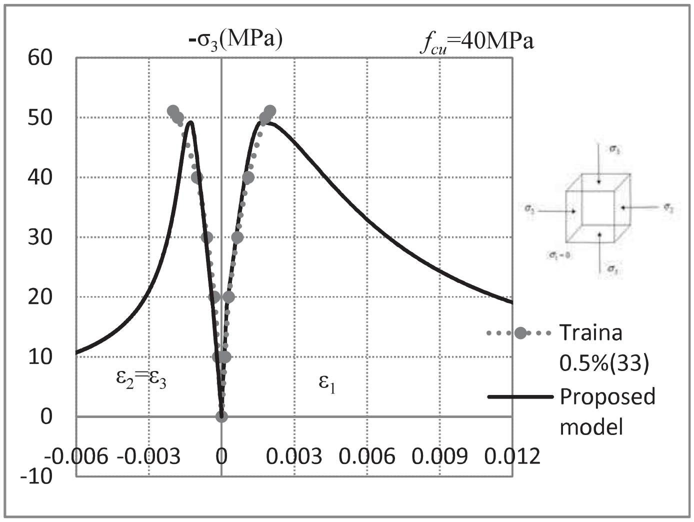

Fig.20 Compression with Traina et al., (1991)

Figure 21
Click here to download Figure: Fig 21.pdf

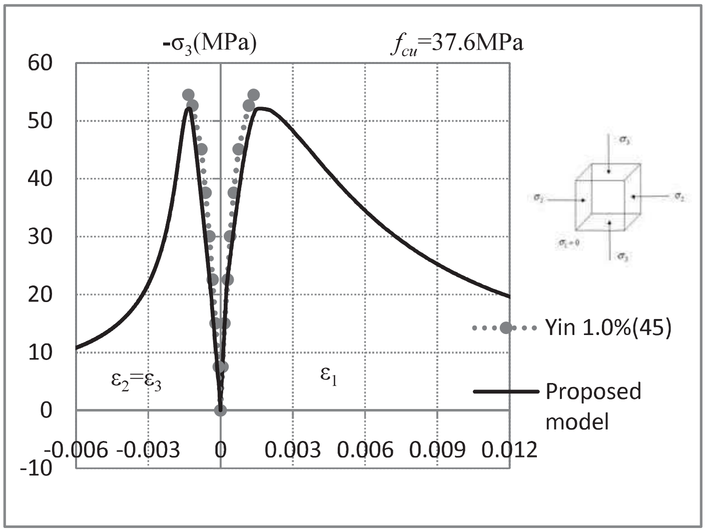

Fig.21 Compression with Yin et al., (1989)

Figure22
Click here to download Figure: Fig 22.pdf

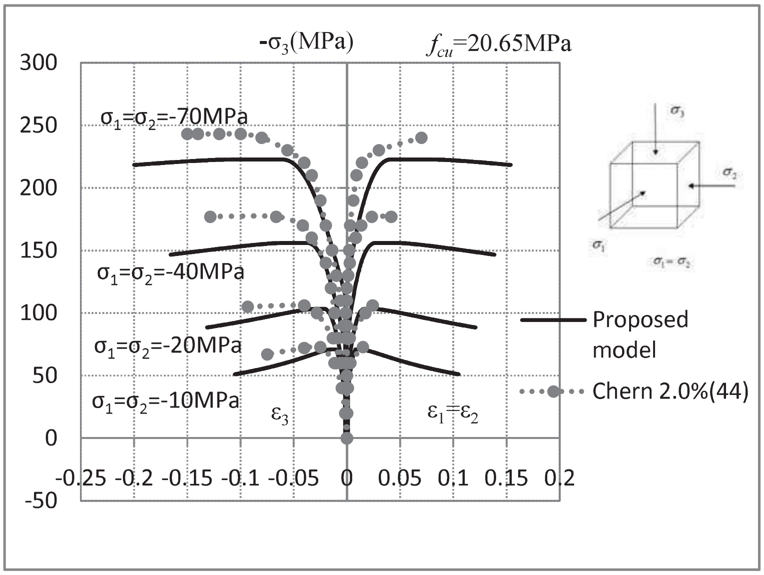

Fig.22Typical experimental results of SFRC under lateral confined triaxial compression are compared with the model prediction